Solution Structure of the Cu(I) and Apo Forms of the Yeast Metallochaperone, Atx1[†,‡]

Fabio Arnesano, Lucia Banci, and Ivano Bertini*

Magnetic Resonance Center CERM and Department of Chemistry, University of Florence, Via Luigi Sacconi 6, 50019, Sesto Fiorentino, Florence, Italy

David L. Huffman and Thomas V. O'Halloran*

Department of Chemistry and Department of Biochemistry, Molecular Biology, and Cell Biology, Northwestern University, Evanston, Illinois 60208

Received June 27, 2000; Revised Manuscript Received December 6, 2000

ABSTRACT: The ^{1}H NMR solution structure of the Cu(I)-bound form of Atx1, a 73-amino acid metallochaperone protein from the yeast *Saccharomyces cerevisiae*, has been determined. Ninety percent of the ^{1}H and 95% of the ^{15}N resonances were assigned, and 1184 meaningful NOEs and 42 $^3J_{HNH\alpha}$ and 60 $^1J_{HN}$ residual dipolar couplings provided a family of structures with rmsd values to the mean structure of 0.37 ± 0.07 Å for the backbone and 0.83 ± 0.08 Å for all heavy atoms. The structure is constituted by four antiparallel β strands and two α helices in a $\beta\alpha\beta\beta\alpha\beta$ fold. Following EXAFS data [Pufahl, R., Singer, C. P., Peariso, K. L., Lin, S.-J., Schmidt, P. J., Fahrni, C. J., Cizewski Culotta, V., Penner-Hahn, J. E., and O'Halloran, T. V. (1997) *Science 278,* 853−856], a copper ion can be placed between two sulfur atoms of Cys15 and Cys18. The structure of the reduced apo form has also been determined with similar resolution using 1252 meaningful NOEs (rmsd values for the family to the mean structure are 0.67 ± 0.12 Å for the backbone and 1.00 ± 0.12 Å for all heavy atoms). Comparison of the Cu(I) and apo conformations of the protein reveals that the Cu(I) binding cysteines move from a buried site in the bound metal form to a solvent-exposed conformation on the surface of the protein after copper release. Furthermore, copper release leads to a less helical character in the metal binding site. Comparison with the Hg(II)−Atx1 solid-state structure [Rosenzweig, A. C., Huffman, D. L., Hou, M. Y., Wernimont, A. K., Pufahl, R. A., and O'Halloran, T. V. (1999) *Structure 7,* 605−617] provides insights into the copper transfer mechanism, and a pivotal role for Lys65 in the metal capture and release process is proposed.

Copper, an essential trace metal, is utilized as a cofactor in variety of redox and hydrolytic proteins. In eukaryotes, copper-dependent metalloenzymes are found in multiple cellular locations, including the cytosol, mitochondria, and cell surface (*1*). Excess copper, however, is highly toxic to most organisms (*1*, *2*). It is not surprising that the transport and sequestration of copper must be tightly controlled.

Until recently, it was not known how copper enzymes obtained their essential cofactors. A new class of metal ion receptor proteins, called metallochaperones, deliver copper to specific intracellular targets (for a recent review, see ref *3*). Recent studies indicate that a principle difficulty is faced by metallochaperones as they deliver copper to the correct intracellular destination: the cytoplasm has a significant thermodynamic overcapacity for copper chelation (*4*). This has led to the suggestion that metallochaperones act like enzymes to lower the activation barrier for copper transfer to specific partners (*5*).

Copper chaperone proteins isolated to date were first identified in the baker's yeast *Saccharomyces cerevisiae*, and homologues have been noted in *Arabidopsis thaliana*, *Caenorhabditis elegans*, *Enterococcus hirae*, mice, and humans (*6*−*13*). The prototypical copper chaperone, Atx1, conducts Cu(I) through the cytoplasm and transfers this cargo directly to a specific partner protein (*5*, *7*, *14*). A functionally related protein is the copper chaperone for superoxide dismutase (CCS) (*15*), which delivers copper to copper−zinc superoxide dismutase 1 (SOD1) in the cytosol (*4*). One of the domains of CCS is a structural homologue of Atx1 (*16*). The Cox17 protein, which is involved in activation of the mitochondrial copper-dependent enzyme cytochrome oxidase (*10*, *17*), may also function as a metallochaperone, but is not homologous to Atx1.

Both the yeast Atx1 and the human Atx1 homologue (HAH1 or ATOX1) specifically transport copper to the secretory pathway for incorporation into copper enzymes destined for the cell surface or extracellular milieu (*7*, *9*, *18*). The target of copper delivery by Atx1 is a P-type copper

[†] This work was supported by the European Community (Contract HPRI-CT-1999-00009), by Italian CNR (Progetto Finalizzato Biotecnologie 99.00286.PF49), and by MURST-ex 40%.

[‡] The average minimized structures of the Cu(I)− and apo-Atx1 proteins are available at the Protein Data Bank: Cu(I)-Atx1, PDB entry 1FD8 and RCSB ID RCSB011496; apo-Atx1, PDB entry 1FES and RCSB ID RCSB011521.

* To wom correspondence should be addressed. I.B.: CERM and Department of Chemistry, University of Florence, Via L. Sacconi, 6-Sesto Fiorentino, Italy; fax, +39 055 4574271; telephone, +39 055 4574272; e-mail, bertini@cerm.unifi.it. T.V.O.: fax, (847) 491-7713; telephone, (847) 491-5060; e-mail, t-ohalloran@nwu.edu.

10.1021/bi0014711 CCC: $20.00
Published on Web 01/20/2001

transporting ATPase, called Ccc2, present in a late Golgi compartment (*7*, *19*). Ccc2 is the yeast homologue of the human Wilson and Menkes copper transporter (*20*−*22*). Atx1 was originally identified as an antioxidant molecule (hence the name Atx1) capable, when present in high copy number, of suppressing oxidative damage in yeast lacking the *SOD1* gene (*6*). Recent studies indicate, however, that the antioxidant chemistry of Atx1 is not catalytic, leaving the copper trafficking as its primary function (*14*).

The NMR structures of MerP, a mercury resistance protein (*23*), and an Atx1-like domain of the Menkes transporter (*24*), have been obtained. The crystal structure of the oxidized (disulfide) apo and Hg(II) forms of Atx1 have also been determined (*25*), as has the NMR structure of the apo form of CopZ, a bacterial protein homologous to Atx1 (*26*). In none of these cases have the structures of the native, Cu(I)-loaded form of the proteins been reported at high resolution. Both the MerP solution structure and the Atx1 crystal structure contain linear Hg(II) as the metal ion, and the structure of the Atx1-like domain of the Menkes transporter was determined with bound Ag(I). Introduction of copper salts into samples of CopZ leads to broadening of the NMR signals of the first loop and the N-terminal part of the first helix (*26*) which prevented structural analysis of the copper binding site. Relaxation studies on copper-bound CopZ showed an increased rotational correlation time compared with that of apo-CopZ, indicating self-aggregation of the protein upon interaction with copper (*26*).

In vitro and two-hybrid assays clearly indicate that contact between Atx1 and its physiological partners is a copper-dependent event (*5*, *7*); however, the molecular mechanisms of partner−protein recognition, metal ion capture, and the subsequent release steps have not been established. Metal-dependent conformational changes in Atx1 are likely to play a role; however, few structural differences have been observed for Atx1 or related proteins. We have undertaken a comparison of the solution structures of the native Cu(I) and the reduced apo form of *S. cerevisiae* Atx1 and found that copper release involves a series of structural changes. These results, when considered with conformational differences between the crystalline Hg−Atx1 structure, lead to new insights into the mechanism of metal transfer.

MATERIALS AND METHODS

Sample Isolation and Preparation. Atx1 was uniformly labeled with ^{15}N by expressing the protein in *Escherichia coli* strain BL21(DE3) (Novagen) and transformed with pET11dAtx1 (*7*), in minimal medium supplemented with $^{15}NH_4Cl$. The protein was isolated by freeze−thaw extraction of the cell pellet and purified to homogeneity by DEAE-Sephacel batch treatment, followed by chromatography on Superdex75 (Pharmacia). The yield of labeled protein was 25 mg/L of culture. The N-terminal Met was processed in *E. coli*, yielding a 72-amino acid protein. The numbering of residues however uses the first codon (Met) as residue 1.

All NMR samples were prepared under a nitrogen atmosphere at 12 °C in a VacAtmospheres chamber, where they were loaded into 535-PP 5 mm quartz NMR tubes (Wilmad) and capped with latex serum caps. Protein concentrations were determined by the Bradford assay and calibrated as described previously (*5*). The copper concentration was determined by ICP-AES. Electrospray mass spectrometry (ES-MS) of unlabeled samples of apo-Atx1 revealed a single peak of 8088 ± 2 Da, corresponding to the full-length Atx1 (unlabeled) lacking its N-terminal methionine. On the contrary, mass spectra of [^{15}N]apo-Atx1 revealed two peaks of 8184 ± 2 and 8226 ± 2 Da. The first peak corresponds to the full-length [^{15}N]Atx1 lacking the methionine. The second peak corresponds to a minor species having a molecular mass ∼42 Da larger.

The NMR sample of [^{15}N]apo-Atx1 was prepared by exchanging the purified protein into 100 mM sodium phosphate (pH 7) and 10% ^2H_2O via ultrafiltration. The final concentration of the [^{15}N]apo-Atx1 NMR sample was 1.7 mM. Cu(I)-bound Atx1 was prepared as previously described (*5*, *7*) and exchanged by ultrafiltration into 100 mM sodium phosphate (pH 7) and 10% ^2H_2O. The metal-to-protein ratio was 1.0 with a protein concentration of 2.8 mM. The Cu(I)−[^{15}N]Atx1 protein was prepared by adding 0.9 equiv of $[Cu(I)\text{-}(CH_3CN)_4]PF_6$ in CH_3CN to a solution of the apoprotein in 50 mM Tris/MES (pH 8) with stirring. The Cu(I)−[^{15}N]Atx1 sample was then exchanged via ultrafiltration into 100 mM sodium phosphate (pH 7) and 10% ^2H_2O. The final metal-to-protein ratio was 0.9 with a protein concentration of 1.8 mM.

NMR Spectroscopy. The NMR spectra were acquired on Avance 800, 600, and 500 and Ultra Shield 400 Bruker spectrometers operating at proton nominal frequencies of 800.13, 600.13, 500.13, and 400.13 MHz, respectively. A triple-resonance (TXI) 5 mm probe was used with Avance 800, 600, and 500 MHz spectrometers, and a broad band observing probe (BBO) for direct detection of the X nucleus was used with an Avance 400 MHz spectrometer. At 600 MHz also, a broad band inverse probe (BBI) was used. All the probes were equipped with pulsed field gradients (PFG) along the *z*-axis.

On the Cu−Atx1 protein, a TOCSY[1] (*27*, *28*) spectrum was recorded on the 500 MHz spectrometer with a spin-lock time of 100 ms, a recycle time of 1 s, and a spectral window of 14 ppm. A two-dimensional NOESY map (*29*, *30*) was acquired on the 800 MHz spectrometer with a mixing time of 100 ms, a recycle time of 1 s, and a spectral window of 14 ppm. A two-dimensional $^{15}N-^1H$ HSQC (*31*−*33*) spectrum was recorded at 800 MHz with an INEPT delay of 2.66 ms, a recycle time of 1 s, and spectral windows of 14 and 33 ppm for the ^1H and ^{15}N dimensions, respectively. A three-dimensional NOESY−^{15}N HMQC (*34*) experiment was recorded with 160 (^1H) × 88 (^{15}N) × 1024 (^1H) data points on the 600 MHz spectrometer, equipped with the BBI probe. In this experiment, the INEPT delay was set to 5.3 ms, the mixing time was 100 ms, and the carrier frequency was set in the center of the amide proton region, at 8.0 ppm. Spectral windows of 14.0, 14.0, and 33.0 ppm were used for the direct ^1H dimension and the indirect ^1H and ^{15}N dimensions, respectively.

[1] Abbreviations: rmsd, root-mean-square deviation; TOCSY, total correlation spectroscopy; NOE, nuclear Overhauser effect; NOESY, nuclear Overhauser effect spectroscopy; HMQC, heteronuclear multiple-quantum coherence; HSQC, heteronuclear single-quantum coherence; INEPT, insensitive nuclei enhanced by polarization transfer; WATERGATE, water suppression by gradient-tailored excitation; TPPI, time-proportional phase incrementation; WEFT, water-eliminated Fourier transform.

The HNHA experiment (*35*) was performed on the 600 MHz spectrometer, equipped with the BBI probe, to determine the $^3J_{HNH\alpha}$ coupling constants. These were used to obtain constraints for ϕ torsion angles. The spectrum was recorded as a 128 (^{1}H) × 80 (^{15}N) × 2048 (^{1}H) data set using PFG along the *z*-axis. The mixing time was 100 ms. Spectral windows of 14, 14, and 33 ppm were used, respectively, for the direct ^{1}H dimension and the indirect ^{1}H and ^{15}N dimensions.

Two series of 10 ^{15}N−^{1}H ^1J-modulated HSQC experiments to measure the $^1J_{N-H}$ coupling constants (*36*), consisting of 32 and 16 scans, respectively, were performed at 800 MHz with dephasing delays, 2Δ, of 45.2, 46.0, 47.6, 48.8, 50.2, 56.4, 57.8, 58.4, 59.6, and 61.0 ms. One set of experiments, each consisting of 32 scans, was performed at 400 MHz using the same 2Δ values as at 800 MHz plus an experiment with a 2Δ of 63.0 ms. Furthermore, a control experiment was carried out with a dephasing delay of 45.2 ms.

On the ^{15}N-labeled sample of apo-Atx1, a one-dimensional ^{1}H NMR spectrum, a ^{15}N−^{1}H HSQC spectrum, and a two-dimensional NOESY and a TOCSY spectrum were recorded with the same acquisition parameters used for the Cu−Atx1 spectra. Two-dimensional NOESY and a TOCSY spectra were also recorded on the unlabeled sample of apo-Atx1.

For all the experiments, quadrature detection in the indirect dimensions was performed in the TPPI mode (*30*), and water suppression was achieved through the WATERGATE sequence (*37*). All two-dimensional data consisted of 4K data points in the acquisition dimension and of 1K experiments in the indirect dimension.

All three- and two-dimensional spectra were collected at 298 K except where indicated otherwise, processed using the standard Bruker software (XWINNMR), and analyzed on IBM RISC 6000 computers using the XEASY program (*38*).

Constraints Used in Structure Calculations. The peaks used for the structure calculations were integrated in the two-dimensional NOESY map acquired at 298 K in H_2O. Intensities of dipolar connectivities were converted into upper distance limits, to be used as input for structure calculations, by using the approach provided by the program CALIBA (*39*). The calibration curves were adjusted iteratively as the structure calculations proceeded. Stereospecific assignments of diastereotopic protons were obtained using the program GLOMSA (*39*).

$^3J_{HNH\alpha}$ coupling constants were correlated to the backbone torsion angle ϕ by means of the appropriate Karplus curve (*35*). These angles were used as constraints in the DYANA calculations and restrained energy minimization (REM) refinement.

The residual dipolar couplings (rdc) originate from the noncomplete averaging of the dipolar coupling due to the partial orientation of the molecule. They are given by the following equation (cf. ref *40*):

$$\mathrm{rdc} = -\frac{1}{4\pi}\frac{{B_0}^2}{15kT}\frac{\gamma_H\gamma_N h}{4\pi^2 {r_{HN}}^3}\left[\Delta\chi_{ax}^{mol}(3\cos^2\theta - 1) + \frac{3}{2}\Delta\chi_{rh}^{mol}(\sin^2\theta\cos 2\phi)\right] \quad (1)$$

where $\Delta\chi_{ax}^{mol}$ and $\Delta\chi_{rh}^{mol}$ are the axial and rhombic components of the molecular magnetic susceptibility anisotropy tensor, χ^{mol}, respectively, and θ and ϕ are polar coordinates describing the orientation of the N−H bond vector in the (axis) frame of the χ^{mol} tensor. The structural constraints we have used in the present calculations are the differences in rdc values (Δrdc) measured at two different fields (18.7 and 9.4 T in this work). They are given by an equation such as eq 1, where ${B_0}^2$ is substituted with $\Delta{B_0}^2$. The dipolar coupling contribution, Δrdc, to Δ^1J_{HN} must be corrected for the contribution due to the dynamic frequency shift (δ_{DFS}), which constitutes a non-negligible, magnetic field-dependent contribution to the rdc of the ^{1}H−^{15}N ^1J (*36*).

Structure Calculations. Structure calculations were performed using the program DYANA (*41*). The copper ion was included in the calculations by adding a new residue in the amino acid sequence, formed by a chain of dummy atoms which have their van der Waals radii set to zero so that the chain can freely penetrate into the protein and one atom with a radius of 1.4 Å, which mimics the copper ion. The sulfur atoms of Cys15 and Cys18 were linked to the metal ion through upper distance limits of 2.5 Å. This approach does not impose any fixed orientation on the ligands with respect to the copper.

In all structure calculations, the relative weight of all classes of constraints (NOE, *J* couplings, and Δrdc) was kept equal to the default DYANA value. A routine implemented in DYANA has been used to include Δrdc constraints in the structure calculations (*42*). The program needs the $\Delta\chi_{ax}^{mol}$ and $\Delta\chi_{rh}^{mol}$ values as input parameters for the structure calculations, while the orientation of the χ^{mol} tensor in the molecular frame is adjusted by the program to minimize the target function. The magnetic susceptibility tensor parameters are obtained by best fitting the experimental Δrdc values to eq 1, by using as input the structural model calculated without their inclusion. The minimized quantity is the square of the difference between calculated and experimental Δrdc values, introducing a tolerance of 0.05 Hz which roughly corresponds to the mean value of the experimental error.

Two hundred random conformers were annealed in 10 000 steps using the constraints described above. The 35 conformers with the lowest target function constitute the final family.

REM was then applied to each member of the family using the AMBER 6 package (*43*). The structural constraints were applied within the molecular mechanics and dynamics module of SANDER, and the Δrdc values were included as constraints by means of the DIPOLE module. The force field parameters for the copper(I) ion were taken to be like they are in similar systems (*44*). In particular, no constraint on the S(Cys15)−Cu−S(Cys18) angle was used. The values of NOE, torsion angle, and Δrdc potentials were calculated with force constants of 50 kcal mol^{-1} Å^{-2}, 32 kcal mol^{-1} rad^{-2}, and 1 kcal mol^{-1} Hz^{-2}.

The program CORMA (*45*), which is based on relaxation matrix calculations, was used to back-calculate the NOESY cross-peaks from the calculated structure to check the consistency of the whole procedure. This has also allowed us to assign a few more cross-peaks between already assigned resonances.

The quality of the structure was evaluated in terms of deviations from ideal bond lengths and bond angles and through Ramachandran plots obtained using the programs

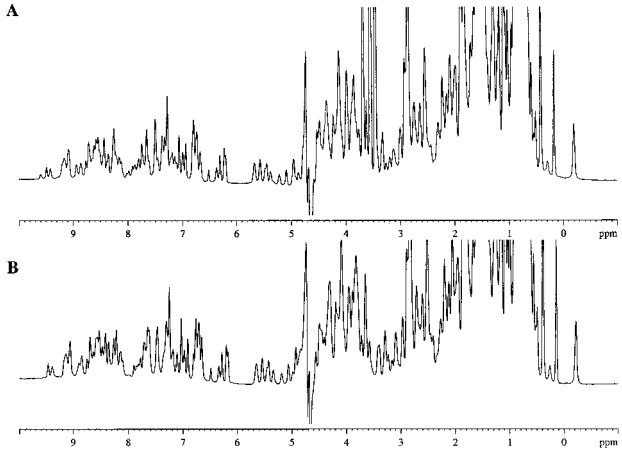

FIGURE 1: ^{1}H NMR 800 MHz spectra of Cu−Atx1 (A) and reduced apo-Atx1 (B) proteins at 298 K and pH 7.0 in 100 mM phosphate buffer. The protein concentrations were 1.8 mM.

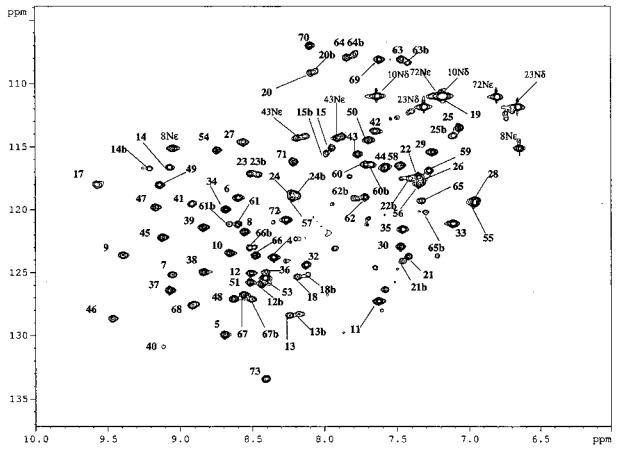

FIGURE 2: ^{1}H−^{15}N HSQC spectrum of the Cu−Atx1 protein at 298 K and pH 7.0 in 100 mM phosphate buffer. Cross-peaks of the minor species of the protein are indicated with a "b". There are at least three weak unassigned peaks in the spectrum. Two of them have variable intensities in HSQC spectra recorded on different protein samples; one peak is real but does not show connectivities.

PROCHECK (*46*) and PROCHECK-NMR (*47*). Solvent accessibility was calculated with the program MOLMOL (*48*) for each structure of the family, and the reported value represents the average.

Structure calculations and analysis were performed on IBM RISC 6000 computers.

RESULTS

Sequence-Specific Assignment of the Cu(I)−Atx1 Protein. A ^{1}H 800 MHz NMR spectrum of Cu−Atx1 is reported in Figure 1A. The assignment of the protein signals was performed by three-dimensional NOESY−^{15}N HMQC and two-dimensional NOESY and TOCSY maps. The TOCSY map was used to identify spin patterns of intraresidue connectivities of the different amino acids. Then, these residues were connected to other spin patterns by sequential characteristic NOESY peaks. The three-dimensional map was used to solve problems of cross-peak overlap in the two-dimensional NOESY map and to assign the ^{15}N resonances. The N-terminal Met was processed in *E. coli*, yielding a 72-amino acid protein. The numbering of residues however uses the first codon (Met) as residue 1. Signals of 70 of 72 residues have been assigned. Residues 2 and 16 have not been identified. The ^{15}N HSQC spectra were recorded also at a low temperature (278 K) in an attempt to identify the missing NHs, but without success. Approximately 93% of the proton resonances could be located in the maps, and 67 of 70 ^{15}N backbone amide resonances (neglecting Pro31 and Pro52 without amide resonances) have been assigned. The amide resonances are missing for residues 2, 3, and 16. The ^{1}H and ^{15}N resonance assignment is reported in the Supporting Information, and the ^{15}N HSQC spectrum of the Cu−Atx1 protein is reported in Figure 2.

Two sets of signals can be detected for 19 NH amide proton resonances (12−15, 18, 20−25, and 60−67). The relative intensity is 2:1. Mass spectra of [^{15}N]apo-Atx1 revealed two peaks corresponding to the full-length [^{15}N]-Atx1 lacking its N-terminal methionine and to a minor species with an ∼42 Da larger molecular mass. This latter species is absent in unlabeled samples of apo-Atx1: mass spectra (ES-MS) recorded on various samples consistently exhibited a single peak, and indeed, two-dimensional maps do show a single set of signals which have the same ^{1}H shifts as the major form of the labeled protein (A form hereafter). In this paper, we report the structural characterization of the Cu(I)-bound and reduced apo state of the A form of the protein.

Secondary Structure from NMR Data. The elements of secondary structure can already be identified by analyzing the pattern of assigned NOEs (*49*). Short- and medium-range NOEs were used to generate Figure 3A. The diagram of long-range connectivities is shown in Figure 3B. In the present protein, two elements of α helical secondary structure can be predicted, which are characterized by a large number of sequential and medium-range connectivities such as $d_{NN}(i,i+1)$, $d_{NN}(i,i+2)$, $d_{\alpha N}(i,i+3)$, $d_{\alpha N}(i,i+4)$, and $d_{\alpha\beta}(i,i+3)$. They involve residues 17−30 and 54−63. These are termed helices α1 and α2 (*25*). From long-range connectivities, as shown in Figure 3B, four antiparallel β strands ($\beta1-\beta4$) can be predicted which correspond to stretches of residues 5−11, 35−39, 44−49, and 66−73.

These secondary structure elements, connected by loop regions, produce the classical "ferredoxin-like" $\beta\alpha\beta$ folding (*50*), a tertiary structure common in many metallochaperone proteins (*23*−*25*).

Solution Structure Calculations and Analysis. In total, 2425 NOESY cross-peaks were assigned and integrated. These were transformed into upper distance limits with the program CALIBA (*39*) and resulted in 1525 unique upper distance limits, of which 1184 meaningful.[2] To ensure equivalent calibration of all cross-peaks (degenerate and nondegenerate), their intensities were normalized by knowing that the ratio between the two forms of the protein is 2:1. The program CORMA (*45*) was used to back-calculate the NOESY cross-peaks from the calculated structure to check the consistency of the whole procedure. This has also allowed us to discriminate between cross-peaks corresponding to forms A and B.

The number of NOEs per residue is reported in Figure 4A. The average number of NOEs per residue is 21, of which

[2] Nonmeaningful distance constraints are those which cannot be violated in any structure conformation and those involving proton pairs at a fixed distance.

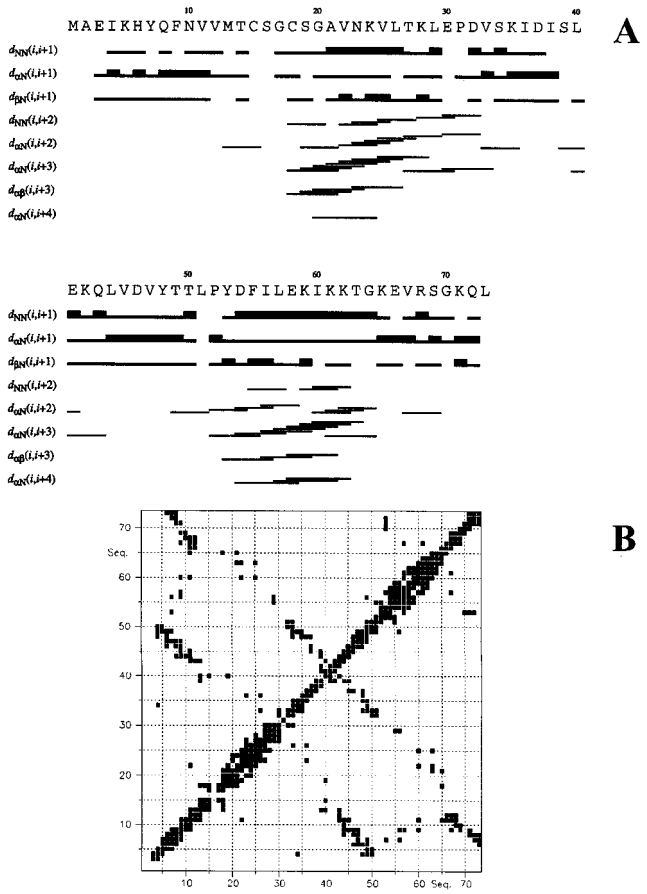

FIGURE 3: (A) Schematic representation of the sequential and medium-range NOE connectivities involving NH, Hα, and Hβ protons of the Cu−Atx1 protein. The thickness of the bar indicates the intensity of NOEs. (B) Schematic representation of long-range connectivities of the Cu−Atx1 protein. Segments perpendicular to the diagonal of the plot represent pairs of antiparallel β strands.

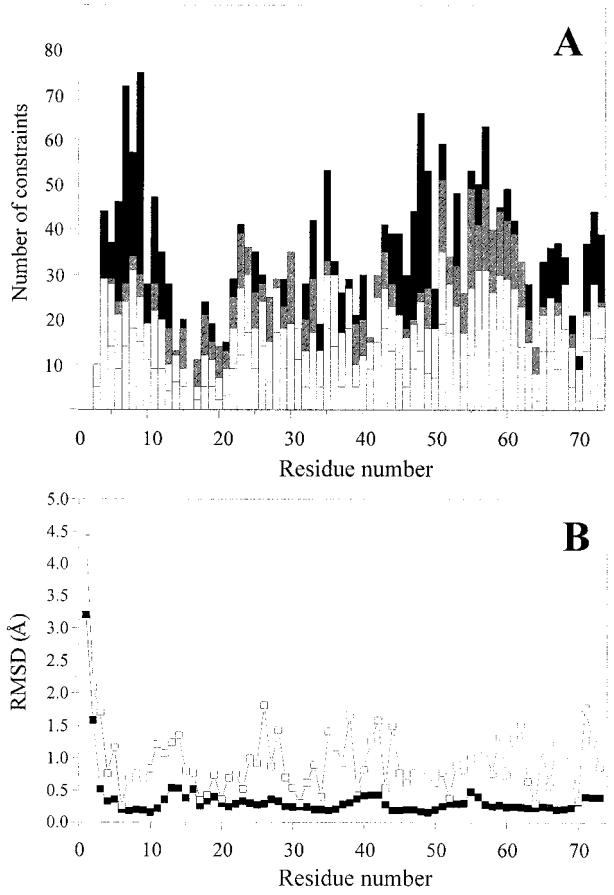

FIGURE 4: (A) Number of meaningful NOEs per residue for the Cu−Atx1 protein. White, shaded, gray, and black bars indicate intraresidue, sequential, and medium- or long-range connectivities, respectively. (B) rmsd per residue to the mean structure of the Cu−Atx1 protein for the backbone (■) and all heavy atoms (□) of the REM structure family of 35 conformers.

16 are meaningful. Forty-two $^3J_{HNH\alpha}$ couplings were obtained from the HNHA three-dimensional spectrum, and 60 Δrdcs were measured. In total, 1286 constraints were used in the structure calculations. For $J_{HNH\alpha}$ values >8 and <4.5 Hz, the ϕ angle was assumed to be between −155° and −85° and between −80° and −30°, respectively. The $^1J_{HN}$ couplings were measured at 800 and 400 MHz, and their values are given in the Supporting Information. The root-mean-square difference between the results of the two sets of experiments recorded at 800 MHz was 0.05 Hz. This value is comparable to those previously reported for other systems (*36*, *51*) and is an estimate of the random error. This precision permits reliable measurements of the small changes (<0.5 Hz) in $^1J_{NH}$ occurring when the magnetic field strength is increased. Furthermore, a systematic error between the experiments at 800 and 400 MHz may also be present. The Δrdc values require a correction, due to a dynamic frequency shift (δ_{DFS}). δ_{DFS} values depend on the rotational regime of the molecule (*36*, *52*). The relative values of the principal components of the inertia tensor of the Cu−Atx1 protein have been estimated from initial structural data and are 1, 0.91, and 0.60. The rotational diffusion tensor (**D**) of the Cu−Atx1 protein is thus expected to be nonisotropic and essentially axially symmetric. In this case, the value of δ_{DFS} depends on the relative orientations of the diffusion and CSA tensors and on the orientation of the NH bond vector with respect to the two tensors (*36*, *52*). Δrdc constraints were used together with all the other constraints since the beginning of structural calculations. The initial values of the axial and rhombic anisotropies of the magnetic susceptibility χ^{mol} tensor were estimated using a preliminary family of 20 conformers obtained using only the NOE constraints. The convergence was reached after two cycles of calculations (the tensor had been recalculated after the first cycle of annealing), and the program yielded a family of conformers consistent with all the experimental constraints. A total of 42 proton pairs were stereospecifically assigned with the program GLOMSA (*39*). The constraints used for structure calculations and the obtained stereospecific assignments are reported in the Supporting Information.

The 35 conformers constituting the final DYANA family have an average target function of 0.88 ± 0.14 Å^2 (the NOE constraints contribute for 0.28 Å^2 and Δrdc constraints for 0.40 Å^2) and an average rmsd to the mean structure (for residues 4−73) of 0.39 ± 0.08 Å for the backbone and 1.10 ± 0.16 Å for all heavy atoms. The mean deviation between calculated and experimental Δrdc values is smaller for the families obtained including the new Δrdc constraints than that for the initial families obtained without these constraints, and the *R*-factors (*53*) are 0.11 and 0.36, respectively, indicating that there has been a reorganization of the protein structure to better satisfy the Δrdc constraints. The final

Table 1: Statistical Analysis of the REM Family and of the Mean Structure of the Cu−Atx1 Protein from *S. cerevisiae*[a]

	REM (35 structures)	⟨REM⟩ (mean)
RSM violations per experimental distance constraint (Å)[b]		
intraresidue (335)	0.0152 ± 0.0015	0.0154
sequential (323)	0.0074 ± 0.0017	0.0066
medium-range[c] (200)	0.0070 ± 0.0018	0.0067
long-range (326)	0.0100 ± 0.0013	0.0095
total (1184)	0.0108 ± 0.0008	0.0106
average no. of NOE violations per structure		
intraresidue	14.8 ± 2.5	16
sequential	4.2 ± 1.5	4
medium-range[c]	1.8 ± 0.9	1
long-range	6.0 ± 1.5	6
total	26.9 ± 3.7	27
average no. of NOE violations larger than 0.3 Å	0	0
largest residual NOE violation (Å)	0.18	0.13
average NOE penalty function (kJ mol^{-1})	37 ± 5	35
42 ϕ angle constraints from $^3J_{HNH\alpha}$ couplings		
average no. of ϕ violations larger than 5°	0.5 ± 0.8	2
average ϕ penalty function (kJ mol^{-1})	2 ± 1	3
60 Δrdcs from $^1J_{HN}$ couplings		
average Δrdc penalty function (kJ mol^{-1})	7.2 ± 0.6	7.3
structural analysis[d]		
% of residues in disallowed regions	0.0	0.0
% of residues in generously allowed regions	2.7	1.5
% of residues in allowed regions	12.8	13.8
% of residues in most favorable regions	84.5	84.7

[a] REM indicates the energy-minimized family of 35 structures; ⟨REM⟩ is the energy-minimized mean structure obtained from the coordinates of the individual REM structures. [b] The number of experimental constraints for each class is reported in parentheses. [c] Medium-range distance constraints are those between residues *i* and *i* + 2, *i* and *i* + 3, *i* and *i* + 4, and *i* and *i* + 5. [d] Results from the Ramachandran plot analysis.

parameters are as follows: $\Delta\chi_{ax}^{mol} = -0.83 \times 10^{-32}$ m^3 and $\Delta\chi_{rh}^{mol} = 0.04 \times 10^{-32}$ m^3. These values are comparable to those previously reported for other diamagnetic systems with nonspherical symmetry (*36*, *54*).

Each conformer of the family was then subjected to further refinement with the program AMBER (*43*). The family has a total penalty function of 46 ± 6 kJ mol^{-1}. The average rmsd values for the family are 0.37 ± 0.07 Å for the backbone and 0.83 ± 0.08 Å for all heavy atoms. The rmsd values per residue to the mean structure of the final REM family are shown in Figure 4B.

The family of conformers was analyzed with PROCHECK-NMR (*47*), and the results of the analysis are reported in Table 1. According to this program, the following secondary structure elements were found: residues 5−12 (β1), 17−30 (α1), 35−39 (β2), 44−49 (β3), 52−63 (α2), and 66−73 (β4), which are completely consistent with the analysis of the NOE patterns, as discussed before.

To assess the conformation of the coordination site of copper(I), calculations were also performed without inclusion of links with the copper ion. In this structure, the conformation of the two cysteines was close to that observed for the refinements that include copper ion, thus indicating that the cysteine conformation in the Cu−Atx1 protein is well defined by the experimental structural constraints.

In Figure 5A, a 35-conformer family of Cu−Atx1 proteins is represented as a tube, whose radius is proportional to the backbone rmsd of each residue. The data presented in Figures 4B and 5 indicate that the largest backbone rmsd values are obtained for residues 2, 3, 13, 14, and 16; the rest of the protein is, on the contrary, well defined with an average backbone rmsd well below 0.4 Å. The higher rmsd values of residues in loop 1 are due to the paucity of NOEs in this region (Figure 4A). This region is an external part of the protein, intrinsically experiencing a small number of NOEs, also because its residues (Thr, Cys, Ser, and Gly) have short side chains. In addition, this region contains Ser16, which has not been identified and therefore produces a break in the sequential connectivities.

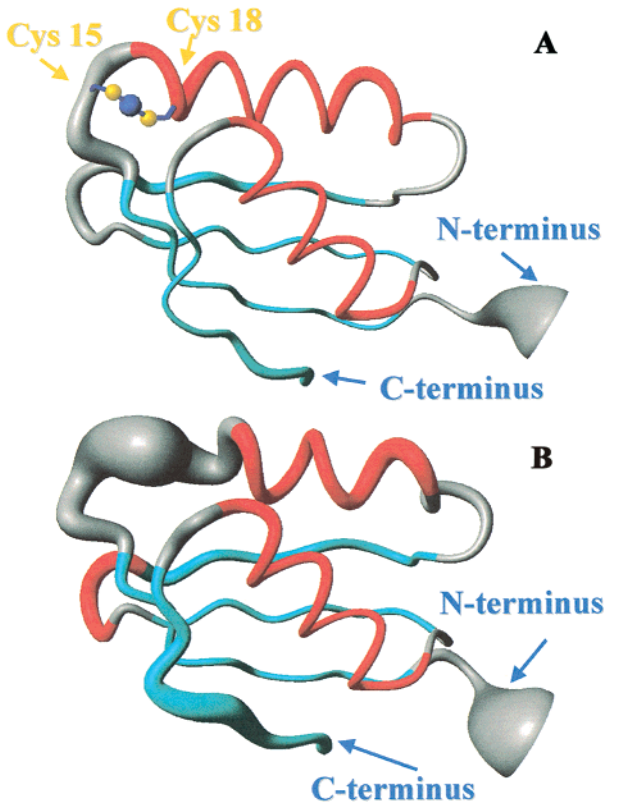

FIGURE 5: Backbone atoms for the solution structures of Cu−Atx1 (A) and apo-Atx1 (B) proteins as a tube with a variable radius, proportional to the backbone rmsd of each residue. Helices are in red and β-strands in cyan. The copper atom (blue) and the sulfur atoms (yellow) of Cys15 and Cys18 are shown. This figure was generated with the program MOLMOL (*48*).

Stability of the Cu(I)−Atx1 Protein. Cu−Atx1 samples are not stable if the concentration of the protein in solution [100 mM phosphate buffer (pH 7)] is higher than 2 mM. Under these conditions, we observed the formation of a precipitate when the temperature of the protein sample is increased from 277 to 298 K. One- and two-dimensional NOESY and TOCSY spectra of the supernatant solution exhibited peaks due to residues belonging to secondary structure elements, while signals from other parts of the molecule are not visible, probably due to a high degree of disorder and to exchange processes of NH amide protons with solvent. These regions, from comparison with the assignment of the native form, include loop regions (26, 28, 29, and 40) and the residues near the copper binding region (13−19 and 21). On the contrary, the Cu−Atx1 protein at concentrations of ≤1.8 mM at 298 K is very stable under an N_2 atmosphere in serum-capped tubes. This is demonstrated by the one-dimensional ^{1}H NMR spectra (see Figure 1A) which remain constant even if recorded after several months.

Structural Characterization of Reduced Apo-Atx1. In Figure 1, the ^{1}H NMR spectrum of the Cu−Atx1 protein is compared with that of the apoprotein. The two spectra are very similar in the methyl and methylene region. Some differences are present in the NH region due to small shifts and to disappearance of some resonances. Inspection of the ^{15}N HSQC map recorded for the apoprotein (data not shown) at 298 K and comparison with the analogous spectrum of the Cu(I) protein show that cross-peaks assigned to amide protons of residues 14 and 16−18 are not present. Other residues (9, 12, 13, 15, 20−22, and 26) display a change (larger than 0.2 ppm) in the ^{15}N shift. Again, two sets of signals can be detected in the ^{15}N-labeled sample for the same amide NHs as in the ^{15}N Cu−Atx1 spectrum. The assignment of the major A form has been performed through the analysis of two-dimensional TOCSY and NOESY maps and of the ^{1}H−^{15}N HSQC spectrum. Signals of 68 of 72 residues have been located. Residues 2 and 16−18 and NHs of Glu3 and Thr14 have not been identified at 298 K. HSQC, NOESY, and TOCSY spectra of apo-Atx1 were also recorded at 278 K in an attempt to identify missing resonances. The NH of Thr14 and the whole pattern of Cys18 were assigned at this temperature. The Hα protons of Gly17 were also tentatively assigned through Hα−HN(i,i+1) dipolar connectivities. With the exception of the latter signals, the others are sizably shifted with respect to the corresponding peaks in the Cu−Atx1 protein. Approximately 90% of the proton resonances could be located in the maps at 298 K. The ^{1}H and ^{15}N resonance assignment is reported in the Supporting Information for both 298 and 278 K measurements.

The pattern of the assigned NOEs indicates the presence of the same secondary structure elements as in the Cu−Atx1 protein except for helix α1, which is shortened from residues 17−30 to 21−28. The absence, even at low temperatures, of strong sequential and medium-range connectivities, characteristic of α helical secondary structure, for residues 17−20 in apo-Atx1 indicates that these residues are not involved in an α helical structure.

In total, 2380 NOESY cross-peaks were assigned and integrated. These were transformed into 1568 unique upper distance limits, of which 1252 are meaningful. The average number of NOEs per residue is 22, of which 17 are meaningful. A total of 38 proton pairs were stereospecifically assigned with the program GLOMSA (*39*).

The 35 conformers constituting the final DYANA family have an average target function of 0.82 ± 0.18 Å^2 and an average rmsd to the mean structure (for residues 4−73) of 0.68 ± 0.13 Å for the backbone and 1.00 ± 0.12 Å for all heavy atoms.

Each conformer of the family was then subjected to further refinement with the program AMBER (*43*). The family has a total penalty function of 30 ± 4 kJ mol^{-1}, corresponding to an average target function of 0.15 Å^2. The average rmsd values for the family are 0.67 ± 0.12 Å for the backbone and 1.00 ± 0.12 Å for all heavy atoms. The quality of the structure is provided by the parameters reported in Table 2.

The family of conformers was analyzed with PROCHECK-NMR (*47*). According to this program, the following secondary structure elements were found: residues 5−12 (β1), 21−28 (α1), 33−39 (β2), 44−49 (β3), 52−63 (α2), and 66−73 (β4). In addition, a 3_{10} helix was found for residues 40−42.

Table 2: Statistical Analysis of the REM Family and of the Mean Structure of Apo-Atx1 from *S. cerevisiae*[a]

	REM (35 structures)	⟨REM⟩ (mean)
RSM violations per experimental distance constraint (Å)[b]		
intraresidue (334)	0.0134 ± 0.0017	0.0130
sequential (316)	0.0073 ± 0.0018	0.0103
medium-range[c] (203)	0.0040 ± 0.0026	0.0050
long-range (399)	0.0060 ± 0.0012	0.0054
total (1252)	0.0088 ± 0.0009	0.0092
average no. of NOE violations per structure		
intraresidue	15.3 ± 2.6	15
sequential	4.0 ± 1.6	5
medium-range[c]	1.3 ± 1.0	1
long-range	4.2 ± 1.4	4
total	24.8 ± 3.2	25
average no. of NOE violations larger than 0.3 Å	0	0
largest residual NOE violation (Å)	0.19	0.13
average NOE penalty function (kJ mol^{-1})	30 ± 4	30
structural analysis[d]		
% of residues in disallowed regions	3.5	3.1
% of residues in generously allowed regions	2.0	3.1
% of residues in allowed regions	20.2	12.3
% of residues in most favorable regions	74.2	81.5

[a] REM indicates the energy-minimized family of 35 structures; ⟨REM⟩ is the energy-minimized mean structure obtained from the coordinates of the individual REM structures. [b] The number of experimental constraints for each class is reported in parentheses. [c] Medium-range distance constraints are those between residues i and i + 2, i and i + 3, i and i + 4, and i and i + 5. [d] Results from the Ramachandran plot analysis.

In Figure 5B, a 35-conformer family of apo-Atx1 is represented as a tube, whose radius is proportional to the backbone rmsd of each residue. The largest backbone rmsd values are obtained for residues at the N-terminus and for the region of residues 13−23, containing loop 1 and the beginning of helix α1. This region contains Ser16, Gly17, and Cys18, which are not detected at 298 K. The NOEs observed at 278 K are consistent with the structure of apo-Atx1, calculated at 298 K. However, because these NOEs are measured at a different temperature, they were not included in the calculations.

The region of residues 13−23 is well defined in the oxidized apoprotein (with a disulfide bridge between the Cys15 and Cys18) recently determined by X-ray (*25*), but it is disordered in the reduced X-ray apo structure (A. C. Rosenzweig, personal communication).

DISCUSSION

Intracellular copper trafficking requires partnerships between diffusible metal receptors known as metallochaperone proteins and their targets. While yeast two-hybrid assays indicate a copper-dependent interaction of the Atx1 copper receptor with the membrane-bound intracellular copper transporter Ccc2 (*7*), metal-dependent conformational changes in the Atx1 structure itself have yet to be elucidated. Comparison of the Cu and apo forms of *S. cerevisiae* Atx1 provides such insights and expands the copper capture and release mechanism proposed for this metallochaperone.

Comparison between the Structures of Reduced Apo- and Cu(I)−Atx1 Proteins. The solution structure of the *S. cerevisiae* Cu−Atx1 protein exhibits a βαββαβ fold with the Cu(I) ion coordinated by two cysteine residues, Cys15 (in loop 1) and Cys18 (in helix α1). The overall folding of

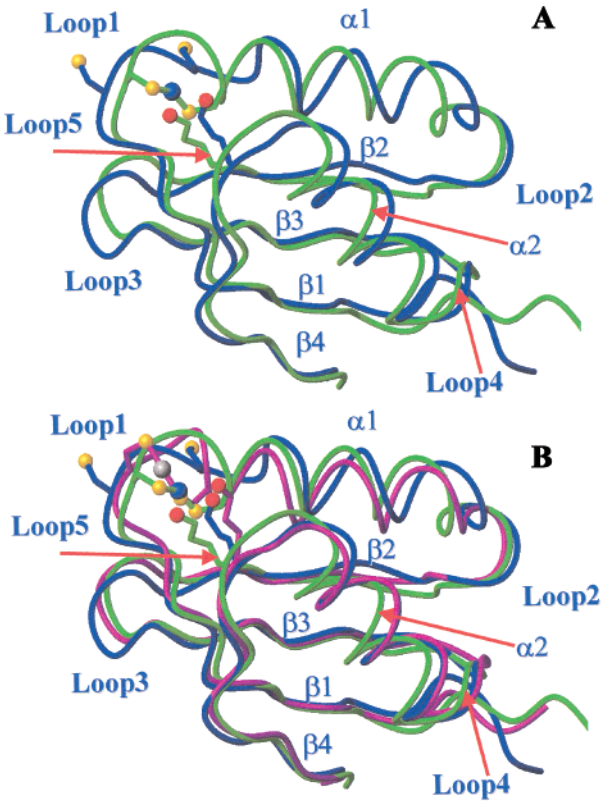

FIGURE 6: (A) Backbone drawing of Cu−Atx1 (green) and apo-Atx1 (blue) proteins. The copper ion is in blue; the sulfur atoms of Cys15 and Cys18 are in yellow, and the Nζ atom of Lys65 is in red. The secondary structure elements are indicated. (B) Backbone drawing of Cu−Atx1 (green), apo-Atx1 (blue), and X-ray Hg−Atx1 (magenta) structures. The copper ion is in blue and the mercury ion in gray; the sulfur atoms of Cys15 and Cys18 are in yellow, and the Nζ atom of Lys65 is in red. The secondary structure elements are indicated.

apo-Atx1 is essentially identical to that observed for the copper- or mercury-bound form of the protein with the exception that helix α1 is shorter by one helical turn at the N-terminus. In Figure 6A, the mean energy-minimized structures of the Cu− and apo-Atx1 structures are superimposed. The global rmsd values for the Cu− and apo-Atx1 pair are 1.53 and 1.96 Å for backbone and all heavy atoms, respectively. The rmsd for backbone atoms per residue is reported in Figure 7 (−•−), and it is compared to the rmsd per residue for each family [apo-Atx1 (•••) and Cu−Atx1 (—)] and the sum of the rmsd values to the mean structure of the two families (- - -). Regions where the rmsd between the two mean minimized structures is larger than the sum of the rmsds of each family indicate conformational differences. The largest backbone rmsd value between the two structures is found for the Cu(I) binding residue, Cys18 (5.86 Å). Sizable differences are also found for residues 15, 19, 25−30, 34−42, 48, and 54−62, the majority of which are in the two α helices.

The conformational differences between the apo- and holoprotein are delineated for each secondary structure element in Table 3, where the rmsd values for the residues in the given secondary structure element are calculated by superimposing either all residues (global rmsd) or three residues at a time (local rmsd). The highest global rmsd values for Cu− versus apo-Atx1 are found for helix α1, strand *β*2, and

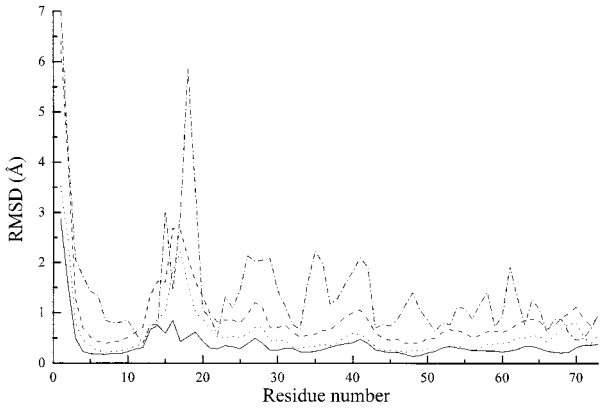

FIGURE 7: rmsd per residue for backbone atoms within the 35-conformer families of the apo-Atx1 (•••) and Cu−Atx1 (—) proteins and between the mean energy-minimized structures of the two families (−•−). The sum of the rmsd values per residue for the two families of structures is also shown (- - -).

loops 1 and 3. The rmsd values for strand *β*2 and loop 3 drop below the average value when the two structures are superimposed locally, indicating that the structural differences in these regions originate from translational displacements of the entire region while the local conformations are well maintained. On the contrary, helix α1 and loop1, which constitute the copper binding region, show a difference also in the local rmsd. This correlates well with the observed changes in the helical character of residues 17−20 (see above).

Copper is bound to the protein through bonds with the sulfur atoms of Cys15 and Cys18. In the Cu−Atx1 protein, loop 1 (containing Cys15) and the beginning of helix α1 (containing Cys18) are well defined (see Figure 5A). The conformation of Cys18 is very similar in all the conformers of the Cu−Atx1 family, while Cys15 is less ordered. Calculations of solvent accessibility on the Cu−Atx1 structure reveal that 25% of the total surface area of Cys15 is exposed to the solvent, while Cys18 is buried with less than 3% accessible surface. In the apo-Atx1 structure, the most dramatic difference is observed for Cys18 which becomes more solvent accessible with ∼45% accessible surface.[3] Cys15 flips from "in" to "out", and the number of residues making up loop 1 increases upon loss of copper. This is confirmed by the fact that, also at low temperatures, there are not the typical connectivities of an α helical structure for residues 17−20 upon release of copper (see above). Amide NHs of residues 17 and 18, belonging to helix α1 in the Cu−Atx1 structure, are not detected at 298 K in apo-Atx1, probably due to solvent exchange and/or to conformational exchange phenomena.

Copper occupancy alters some secondary structure elements more than others. Superposition of the two average structures (Figure 6A) reveals that strands *β*1, *β*3, and *β*4 do not change much upon loss of copper, while a large global rmsd was found for strand *β*2. Helix α2 is ordered to the same extent in both structures but appears to undergo a translational movement. The global rmsd for α2 is larger than the sum of the rmsd values of each family (see Figure

[3] This number should be taken as qualitative as no NOEs are available for Cys18 of apo-Atx1. Nevertheless, the backbone NOEs detected for this residue at 278 K define the Cα−C*β* orientation and are consistent with the family of structures calculated at 298 K.

Table 3: Comparison of the Cu(I)−Atx1 Solution Structure with the Reduced Apo-Atx1 Solution Structure and the Hg(II)−Atx1 X-ray Structure[a]

secondary structure element	residue range	global backbone rmsd between NMR Cu(I)− and apo-Atx1 (Å)	local backbone rmsd between NMR Cu(I)− and apo-Atx1 (Å)	global backbone rmsd between NMR Cu(I)− and X-ray Hg(II)−Atx1 (Å)	local backbone rmsd between NMR Cu(I)− and X-ray Hg(II)−Atx1 (Å)
β1	5−12	0.88	0.18	0.70	0.17
α1	17−30	2.02	0.40	1.13	0.22
β2	35−39	1.65	0.20	0.91	0.16
β3	44−49	1.00	0.20	0.44	0.13
α2	52−63	1.08	0.11	1.25	0.12
β4	66−73	0.70	0.17	0.68	0.18
loop 1	13−16	1.50	0.72	2.09	0.46
loop 2	31−34	1.04	0.30	1.04	0.45
loop 3	40−43	1.60	0.15	0.82	0.16
loop 4	50 and 51	0.74	0.12	1.06	0.14
loop 5	64 and 65	1.17	0.30	1.14	0.30

[a] Backbone rmsd values for each secondary structure element are obtained by superimposing either all residues (global rmsd) or three residues at a time (local rmsd).

7), but the local rmsd is quite small (see Table 3). In particular, helix α2 and loop 5 of apo-Atx1 move away from the copper binding region. The movement of loop 5 is consistent with the change in several long-range NOEs of residues in the helix. For example, in the Cu−Atx1 spectrum, a NOESY cross-peak was identified between the Hβ proton of Val25 (α1) and an Hβ proton of Lys59 (α2). This peak was not detected in the apo-Atx1 spectrum, which displayed in its turn two new cross-peaks between the Hα and Hβ protons of Val25 and the γ-CH_3 group of Thr63 (α2). In apo-Atx1, Ile60 (α2) lost an inter-residue connectivity with Val11 (β1), but two new NOESY cross-peaks are present between the Hβ protons of Phe9 (β1) and the δ-CH_3 group of Ile60. These differences, and other consistent changes in NOE intensities, are consistent with a slight translation of helix α2 as it occurs when passing from Cu− to apo-Atx1.

Other observations suggest that loop 3 is close to loop 1 as long as the metal is bound to the protein. A change in the long-range NOE pattern is also observed for residues 40−43 forming loop 3. For instance, in the Cu−Atx1 spectrum, some NOESY cross-peaks were detected between the side chain protons of Leu40 (loop 3) and the HN and Hα protons of Met13 (loop 1) and the HN and Hβ protons of Ser19 (α1), which are lost in apo-Atx1. In the latter form, there are new peaks between the side chain protons of Leu40 and the HN group of Cys15 (loop 1). In addition, the intensities of cross-peaks between the Hα and Hβ protons of Leu40 and the ϵ-NH group of Gln43 (loop 3) increase when copper is absent.

In the Cu−Atx1 protein, a hydrogen bond is formed between one ϵ-NH group of Gln43 and the carbonyl of Met13, which is not present in the apo structure as demonstrated by the different set of NOEs in this region. These differences are consistent with a translation of loop 3 away from the metal binding loop upon loss of copper. This translation is supported by analysis of Table 3.

Comparison between the X-ray Hg−Atx1 and NMR Cu−Atx1 Structures. The crystal structure of the *S. cerevisiae* Hg−Atx1 protein has been recently determined (*25*). The global rmsd values between the two mean minimized structures are 1.12 and 1.72 Å for backbone and all heavy atoms, respectively. The β sheet and loop 3 are well superimposed (see Table 3), and the highest rmsd values between the two structures are observed for helices and loops 1 and 5. Helix α2 and loop 5 undergo a translation (see Figure 6B), the largest displacements between the two structures occurring for the backbone atoms of residues 54, 61, and 64. In the vicinity of the metal binding region, the side chain of Lys65 has a different position with respect to the metal ion and its Cys ligands. In the Hg(II)−Atx1 crystal structure, the Nζ atom of Lys65 is closer to the sulfur of Cys18 (3.9 Å) than to the sulfur of Cys15 (7.2 Å), while in the mean minimized Cu−Atx1 solution structure, the Nζ is very close to the sulfur of Cys15 (2.9 Å) and is farther from Cys18 (5.0 Å). Cys15 in loop 1 is the residue with the highest backbone rmsd value between the Cu− and Hg−Atx1 structures (3.0 Å), and its side chain points toward loop 5 containing Lys65 when copper is bound. This variation in the conformation of loop 1 in the Cu−Atx1 structure with respect to the Hg−Atx1 structure results in a significantly different position of the metal ion: the mercury ion is closer to the surface than copper.

It is interesting to note that crystallization of the Cu(I)−Atx1 protein was attempted; however, the metal binding loop was disordered, and no ordered copper was observed (*25*). The same disorder was found in the crystals of the reduced apo structure. On the contrary, if Hg is bound or a disulfide bridge is formed between the sulfur atoms of Cys15 and Cys18 as in oxidized apo-Atx1, the loop becomes ordered (*25*). A comparison of the structures of Hg-bound and oxidized apo-Atx1 showed that the metal binding site is able to accommodate both two- and three-coordinated geometries (*25*). Extended X-ray absorption fine structure analysis of the Cu(I)−Atx1 protein similarly indicated that copper(I) is bound to two cysteines with a more distant interaction with a third unidentified ligand, but is also consistent with a mixture of two- and three-coordinate species (*7*).

Copper Coordination Environment. In the Hg−Atx1 protein, the metal coordination is linear as expected for Hg(II) (*55*), while in the present Cu−Atx1 structure family of 35 conformers, there is a spreading in the values of the S−Cu−S angle (120 ± 40°), suggesting that coordination may not be fixed, but Cu(I) probably prefers a coordination number of >2.

X-ray absorption spectra (*7*) indicate that a more distant third atom at 2.4 Å, from either a buffer molecule or a protein

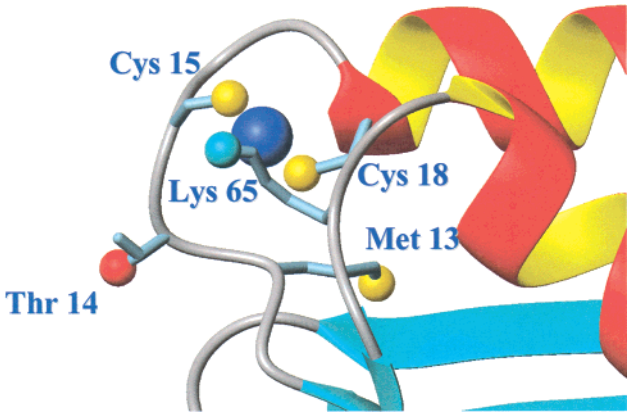

FIGURE 8: Mean minimized solution structure of the Cu−Atx1 protein. Residues in the vicinity of the copper binding site are indicated.

side chain, can also interact with the Cu(I) center. Protein-based atoms that approach copper (see Figure 8) include the Nζ atom of the side chain of Lys65 (Cu−N = 5 ± 1 Å), which belongs to loop 5, or the Oγ atom of Thr14 (Cu−O = 6 ± 1 Å) and Met13 (Cu−S = 7 ± 1 Å). The average positions are not close to the Cu(I) to account for the X-ray absorption data; however, when the Nζ atom of Lys65 is constrained to a Cu−N distance of 2 Å, no structural violations are observed. While this suggests that the protein fold can accommodate a close approach of Lys65 to the copper, it does not resolve the identity of the distant atom in the EXAFS data.

In the Cu−Atx1 protein, Cys15, belonging to loop 1, is more solvent exposed than Cys18, which belongs to helix α1. After the copper release, i.e., when the apoprotein is formed, the amide NH of Cys18 is not detected anymore at 298 K, and this disappearance could be ascribed to exchange with solvent or to conformational exchange phenomena of this residue.[4] On the contrary, the amide NH of Cys15 can still be detected in the NMR spectra of the apo form of the protein. The different trend in signal detectability for Cys18 and Cys15 can indicate that Cys15, which is the most exposed, interacts with Ccc2 when the protein−protein complex is formed, while Cys18 is detached at first from copper coordination in Atx1, thus becoming more mobile.

As mentioned before, two sets of signals are found in the NMR spectra of ^{15}N-labeled samples (see Figure 2) for NH groups of residues belonging to loop 1, helices α1 and α2, and loop 5, due to the presence of two species. A clustering of seven lysine residues, in positions 24, 28, 59, 61, 62, 65, and 71, generates a positively charged face on the molecule, as shown in Figure 9, and five of these residues show a doubling of the signals. In particular, Lys65, which is very close to copper, shows two sets of signals.

Comparison of the Hg−MerP, Apo-CopZ, and Cu−Atx1 NMR Structures. The Cu−Atx1 structure can also be compared with the Hg-bound solution structure of MerP (*23*), a mercury detoxification protein from bacteria (*56*−*59*), and apo-CopZ (*26*), which has been proposed to serve a role like Atx1 in the bacterium *En. hirae* (*60*, *61*). A structure-based

[4] Mobility studies (manuscript in preparation) show that loops 1 and 5 and helices α1 (N-terminus) and α2 (C-terminus) are involved in larger mobility in the millisecond to microsecond time range in the apo form with respect to the holoprotein.

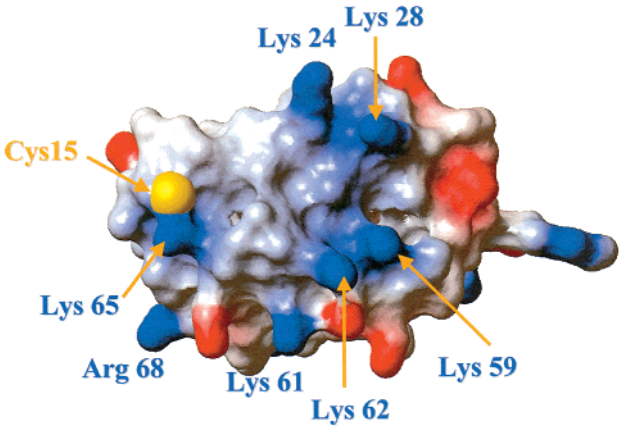

FIGURE 9: Electrostatic surface representation of the copper form of Atx1. The positively charged, negatively charged, and neutral amino acids are represented in blue, red, and white, respectively. The residues that can play a role in molecular recognition and copper transfer are indicated. This figure was generated with the program MOLMOL (*48*).

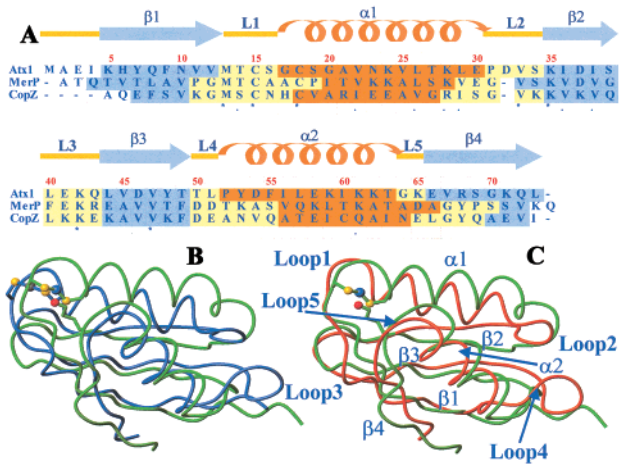

FIGURE 10: (A) Sequence alignment of the Atx1 amino acid sequence with the sequences of other structurally characterized βαββαβ proteins. The positions of the Atx1 secondary structure elements determined from the mean minimized copper-bound solution structure are shown at the top. As noted in the text, helix α1 is shorter by one full turn in the apo form. β strands are in blue, α helices in orange, and loop regions in yellow. Each sequence is shaded according to its secondary structure element as well: Hg(II)−MerP, periplasmic mercury transporter from *Shigella flexinery* (PDB entry 1AFJ); and apo-CopZ, bacterial copper protein from *En. hirae* (PDB entry 1CPZ). Residues that are highly similar or conserved are indicated, respectively, by the symbols • and * below the sequences. (B) Backbone drawing of Cu−Atx1 (green) and Hg−MerP (blue) structures. The copper ion is in blue and the mercury ion in gray; the sulfur atoms of Cys15 and Cys18 are in yellow, and the Nζ atom of Lys65 is in red. (C) Backbone drawing of Cu−Atx1 (green) and apo-CopZ (orange) structures. The secondary structure elements are indicated.

sequence alignment of Atx1 with these proteins is reported in Figure 10A. The protein fold is similar in all cases. The overall backbone rmsd value is 4.4 Å between the Cu−Atx1 and Hg−MerP structures and 4.1 Å between the Cu−Atx1 and apo-CopZ structures. The major structural changes are represented by translations, lengths of the secondary structure elements, and variations in loop size.

Comparison of the Cu−Atx1 and Hg−MerP proteins (Figure 10B) reveals that the largest displacements are found for helix α1 and loops 1 and 3. Loop 1 in the Hg−MerP

structure is extended toward the solvent, and the position of Hg(II) is more external than that of Cu(I), as found in the Hg(II)−Atx1 crystal structure. Intriguingly, both metal binding Cys residues are in loop 1, and helix α1 is shorter in the Hg−MerP structure. Other conformational differences exist in helix α1, loop 3, and loop 5, while the β-sheet is superimposed well.

The structure of the apo form of CopZ is well defined in loop 1 (*26*), at variance with that of the present apo-Atx1 structure. Addition of copper to CopZ led to aggregation and broadening of the signals in loop 1 and prevented any direct structural analysis of the copper binding region (*26*). In contrast, copper makes loop 1 of Atx1 more ordered and less exposed to the solvent. Surprisingly, loops 1 and 3 in apo-CopZ are similar to those of the Cu−Atx1 structure (Figure 10C), suggesting that, unlike apo-Atx1, the metal site in apo-CopZ is preorganized to some extent. This may be related to other significant differences between Atx1 and CopZ, including the surface charge.

Conclusions and Mechanistic Implications. Four remarkable features emerge from comparison of the superimposed structures (see Figure 6B): (i) The β-sheet orientation is unchanged upon metal coordination; however, helix α1 extends by one full turn for both metal-bound structures. (ii) Helix α2 is well superimposed in the apo and Hg structures and is translated with respect to the Cu structure. (iii) Loop 3 (residues 40−43) is similar in the Cu and Hg structures. (iv) Loop 1 becomes more solvent exposed when passing from the Cu− to Hg−Atx1 protein and finally to apo-Atx1. Lys65, the residue on loop 5 closest to loop 1, appears to be pivotal in the metal-induced conformational changes, either attracting or pushing away the sulfur of Cys15. We suggest that the proximity of Lys65 leads to stabilization of the overall negative charge resulting from binding of Cu(I) to two cysteinate anions. In the mercury-bound protein, the charge is neutralized by Hg(II) itself [which bears a 2+ charge instead of the 1+ of Cu(I)], and this further stabilizes the loop after metal binding.

On the basis of these findings, three aspects of a mechanism for Cu release can be hypothesized. First, the metallochaperone is proposed to exist in a *Cu-transiting* form (Cu−Atx1). In this structure, Lys65 is pulled into the active site and helix α2 translates toward the metal center. The Lys65-containing loop 5 protects the sulfur of Cys18 from solvent and covers most of the Cu surface. In this manner, the copper may be protected for incoming oxidants or ligating atoms of nonpartner proteins. Next, we envision that the metallochaperone undergoes a conformational change as a prelude to metal tranfer. This state is similar to the Hg−Atx1 structure. In the Hg−Atx1-like state, Lys65 has moved away from the metal center and so has helix α2, Cys15 is more exposed, and loop 1 lengthens at the expense of helix α1 and begins to fold back. After transfer of the metal ion, the protein is assumed to undergo additional conformational changes, leading to the apo-Atx1 structure. In the apo form, Lys65 is no longer attracted to the now protonated cysteines and helix α2 remains in a similar position as in the pre-metal transfer intermediate. Loop 1 is extended toward the solvent, while loop 3 (residues 40−43) goes away from loop 1.

The stabilization of the protein folding in the Cu−Atx1 structure with respect to the apo form is mainly due to copper(I) coordination by the sulfur atoms of Cys15 and Cys18. In addition, the peptide dipoles of the first turn at the N-terminus of helix α1 and the positive charge of the side chain of Lys65 create a more positive potential which stabilizes the negative charge of the Cu(I) bis-thiolate center. Metal-induced stabilization of helix α1 in the Cu−Atx1 structure, due to a decrease in mobility or in the level of solvent exposure, can be functional. In fact, residues 17−20, constituting the first turn of helix α1, determine an attractive interaction between the field generated by the helix and thiolates, whereas they are not assigned to a helical structure in apo-Atx1. Finally, the approach of Lys65 toward the copper site, favored by a translation of helix α2 in the Cu−Atx1 structure, could represent rearrangement of the protein structure for optimization of electrostatic interactions upon copper binding.

ACKNOWLEDGMENT

We thank Prof. G. Moneti for recording mass spectra on the ^{15}N-labeled apo-Atx1.

SUPPORTING INFORMATION AVAILABLE

The ^{1}H and ^{15}N chemical shifts, the experimental NOE intensities used for the structure calculations, and the list of stereospecific assignments for both Cu(I)− and apo-Atx1 and 42 $^{3}J_{HNH\alpha}$ coupling constants and 60 Δrdc constraints for the Cu(I)−Atx1 protein. This material is available free of charge via the Internet at http://pubs.acs.org.

REFERENCES

1. Linder, M. C. (1991) *Biochemistry of Copper*, Plenum Press, New York.
2. Vulpe, C. D., and Packman, S. (1995) *Annu. Rev. Nutr. 15*, 293−322.
3. O'Halloran, T. V., and Culotta, V. C. (2000) *J. Biol. Chem. 275*, 25057−25060.
4. Rae, T., Schmidt, P. J., Pufahl, R. A., Culotta, V. C., and O'Halloran, T. V. (1999) *Science 284*, 805−808.
5. Huffman, D. L., and O'Halloran, T. V. (2000) *J. Biol. Chem. 275*, 18611−18614.
6. Lin, S., and Culotta, V. C. (1995) *Proc. Natl. Acad. Sci. U.S.A. 92*, 3784−3788.
7. Pufahl, R., Singer, C. P., Peariso, K. L., Lin, S.-J., Schmidt, P. J., Fahrni, C. J., Culotta, V. C., Penner-Hahn, J. E., and O'Halloran, T. V. (1997) *Science 278*, 853−856.
8. Himelblau, E., Mira, H., Lin, S. J., Culotta, V. C., Penarrubia, L., and Amasino, R. M. (1998) *Plant Physiol. 117*, 1227−1234.
9. Klomp, L. W. J., Lin, S. J., Yuan, D., Klausner, R. D., Culotta, V. C., and Gitlin, J. D. (1997) *J. Biol. Chem. 272*, 9221−9226.
10. Amaravadi, R., Glerum, D. M., and Tzagoloff, A. (1997) *Hum. Genet. 99*, 329−333.
11. Odermatt, A., and Solioz, M. (1995) *J. Biol. Chem. 270*, 4349−4354.
12. Wakabayashi, T., Nakamura, N., Sambongi, Y., Wada, Y., Oka, T., and Futai, M. (1998) *FEBS Lett. 440*, 141−146.
13. Nishihara, E., Furuyama, T., Yamashita, S., and Mori, N. (1998) *Mol. Neurosci. 9*, 3259−3263.
14. Portnoy, M. E., Rosenzweig, A. C., Rae, T., Huffman, D. L., O'Halloran, T. V., and Culotta, V. C. (1999) *J. Biol. Chem. 274*, 15041−15045.
15. Culotta, V. C., Klomp, L., Strain, J., Casareno, R., Krems, B., and Gitlin, J. D. (1997) *J. Biol. Chem. 272*, 23469−23472.
16. Lamb, A. L., Wernimont, A. K., Pufahl, R. A., Culotta, V. C., O'Halloran, T. V., and Rosenzweig, A. C. (1999) *Nat. Struct. Biol. 6*, 724−729.

17. Srinivasah, C., Posewitz, M. C., George, G. N., and Winge, D. R. (1998) *Biochemistry 37*, 7572−7577.
18. Hung, I. H., Casareno, R. L., Labesse, G., Mathews, F. S., and Gitlin, J. D. (1998) *J. Biol. Chem. 273*, 1749−1754.
19. Yuan, D. S., Dancis, A., and Klausner, R. D. (1997) *J. Biol. Chem. 272*, 25787−25793.
20. Bull, P. C., and Cox, D. W. (1994) *Trends Genet. 10*, 246−252.
21. Yuan, D. S., Stearman, R., Dancis, A., Dunn, T., Beeler, T., and Klausner, R. D. (1995) *Proc. Natl. Acad. Sci. U.S.A. 92*, 2632−2636.
22. Fu, D., Beeler, T. J., and Dunn, T. M. (1995) *Yeast 11*, 283−293.
23. Steele, R. A., and Opella, S. J. (1997) *Biochemistry 36*, 6885−6895.
24. Gitschier, J., Moffat, B., Reilly, D., Wood, W. I., and Fairbrother, W. J. (1998) *Nat. Struct. Biol. 5*, 47−54.
25. Rosenzweig, A. C., Huffman, D. L., Hou, M. Y., Wernimont, A. K., Pufahl, R. A., and O'Halloran, T. V. (1999) *Structure 7*, 605−617.
26. Wimmer, R., Herrmann, T., Solioz, M., and Wüthrich, K. (1999) *J. Biol. Chem. 274*, 22597−22603.
27. Bax, A., and Davis, D. G. (1985) *J. Magn. Reson. 63*, 207−213.
28. Griesinger, C., Otting, G., Wüthrich, K., and Ernst, R. R. (1988) *J. Am. Chem. Soc. 110*, 7870−7872.
29. Macura, S., Wüthrich, K., and Ernst, R. R. (1982) *J. Magn. Reson. 47*, 351−357.
30. Marion, D., and Wüthrich, K. (1983) *Biochem. Biophys. Res. Commun. 113*, 967−974.
31. Palmer, A. G., III, Cavanagh, J., Wright, P. E., and Rance, M. (1991) *J. Magn. Reson. 93*, 151−170.
32. Kay, L. E., Keifer, P., and Saarinen, T. (1992) *J. Am. Chem. Soc. 114*, 10663−10665.
33. Schleucher, J., Schwendinger, M., Sattler, M., Schmidt, P., Schedletzky, O., Glaser, S. J., Sorensen, O. W., and Griesinger, C. (1994) *J. Biomol. NMR 4*, 301−306.
34. Kay, L. E., Marion, D., and Bax, A. (1989) *J. Magn. Reson. 84*, 72−84.
35. Vuister, G. W., and Bax, A. (1993) *J. Am. Chem. Soc. 115*, 7772−7777.
36. Tjandra, N., Grzesiek, S., and Bax, A. (1996) *J. Am. Chem. Soc. 118*, 6264−6272.
37. Piotto, M., Saudek, V., and Sklenar, V. (1992) *J. Biomol. NMR 2*, 661−666.
38. Eccles, C., Güntert, P., Billeter, M., and Wüthrich, K. (1991) *J. Biomol. NMR 1*, 111−130.
39. Güntert, P., Braun, W., and Wüthrich, K. (1991) *J. Mol. Biol. 217*, 517−530.
40. van Zijl, P. C. M., Ruessink, B. H., Bulthuis, J., and Maclean, C. (1984) *Acc. Chem. Res. 17*, 172−180.
41. Güntert, P., Mumenthaler, C., and Wüthrich, K. (1997) *J. Mol. Biol. 273*, 283−298.
42. Banci, L., Bertini, I., Huber, J. G., Luchinat, C., and Rosato, A. (1998) *J. Am. Chem. Soc. 120*, 12903−12909.
43. Case, D. A., Pearlman, D. A., Caldwell, J. W., Cheatham, T. E., Ross, W. S., Simmerling, C. L., Darden, T. A., Merz, K. M., Stanton, R. V., Cheng, A. L., Vincent, J. J., Crowley, M., Tsui, V., Radmer, R. J., Duan, Y., Pitera, J., Massova, I., Seibel, G. L., Singh, U. C., Weiner, P. K., and Kollman, P. A. (1999) *AMBER 6*, University of California, San Francisco.
44. Banci, L., Benedetto, M., Bertini, I., Del Conte, R., Piccioli, M., and Viezzoli, M. S. (1998) *Biochemistry 37*, 11780−11791.
45. Borgias, B., Thomas, P. D., and James, T. L. (1989) *COmplete Relaxation Matrix Analysis* (*CORMA*), University of California, San Francisco.
46. Laskowski, R. A., MacArthur, M. W., Moss, D. S., and Thornton, J. M. (1993) *J. Appl. Crystallogr. 26*, 283−291.
47. Laskowski, R. A., Rullmann, J. A. C., MacArthur, M. W., Kaptein, R., and Thornton, J. M. (1996) *J. Biomol. NMR 8*, 477−486.
48. Koradi, R., Billeter, M., and Wüthrich, K. (1996) *J. Mol. Graphics 14*, 51−55.
49. Wüthrich, K. (1986) *NMR of Proteins and Nucleic Acids*, Wiley, New York.
50. Hubbard, T. J. P., Murzin, A. G., Brenner, S. E., and Chothia, C. (1997) *Nucleic Acids Res. 25*, 236−239.
51. Tolman, J. R., and Prestegard, J. H. (1996) *J. Magn. Reson., Ser. B 112*, 245−252.
52. Werbelow, L. (1996) in *Encyclopedia of Nuclear Magnetic Resonance* (Grant, D. M., and Harris, R. K., Eds.) pp 1776−1783, John Wiley and Sons, Chichester, U.K.
53. Clore, G. M., and Garret, D. S. (1999) *J. Am. Chem. Soc. 121*, 9008−9012.
54. Tjandra, N., Omichinski, J. G., Gronenborn, A. M., Clore, G. M., and Bax, A. (1997) *Nat. Struct. Biol. 4*, 732−738.
55. Kubicki, M. M., Kergoat, R., Guerchais, J. E., Bkouche-Waksman, I., Bois, C., and L'Hairdon, P. (1981) *J. Organomet. Chem. 219*, 329−343.
56. Foster, T. J. (1987) *CRC Crit. Rev. Microbiol. 15*, 117−140.
57. O'Halloran, T. V. (1993) *Science 261*, 715−725.
58. Brown, N. L. (1985) *Trends Biochem. Sci. 10*, 400−403.
59. Lund, P. A., and Brown, N. L. (1987) *Gene 52*, 207−214.
60. Odermatt, A., Suter, H., Krapf, R., and Solioz, M. (1992) *Ann. N.Y. Acad. Sci. 671*, 484−486.
61. Cobine, P., Wickramasinghe, W. A., Harrison, M. D., Weber, T., Solioz, M., and Dameron, C. T. (1999) *FEBS Lett. 445*, 27−30.

BI0014711